Submission to American Mineralogist: Revision 1

High pressure and temperature equation of state of cobalt oxide: Implications for redox relations in Earth's mantle

Matt Armentrout[1,*], Emma Rainey[1], and Abby Kavner[1]

[1]Department of Earth and Space Science, University of California Los Angeles, Los Angeles, CA 90095

Abstract

The high pressure and temperature equation of state of rock salt-structured cobalt oxide was measured up to 65 GPa and 2600 K using synchrotron X-ray diffraction in conjunction with the laser heated diamond anvil cell. Fitting a Mie-Grüneisen-Debye model to the data we find best fit parameters V_0=77.4 (fixed) Å^3, K_0=190 (1) GPa, K'=3.49 (4), γ_0=1.54 (4), q=2.87 (15), and θ_0=517.8 K (fixed). We use this newly determined equation of state in conjunction with existing measurements of the thermoelastic parameters of cobalt metal to calculate the Gibbs free energy difference between the cobalt oxide and cobalt metal phases as a function of pressure and temperature. A comparison of the energetics of the Co/CoO system with the Ni/NiO system predicts that below 58 GPa CoO+Ni is stable relative to NiO+Co, while above 58 GPa the reverse is true. This tipping point in energy can be mapped as a crossing point in the electrochemical potential of the two metal ions, suggesting that the cobalt becomes more siderophile than nickel with increasing pressure. This result is in qualitative agreement with existing measurements of nickel and cobalt partition coefficients between mantle and core materials.

Keywords: Synchrotron X-ray diffraction; Cobalt oxide; Equation of state; High pressure; Thermoelastic properties; Diamond anvil cell; Laser heating; Redox

1. Introduction

First row transition metals play important roles in the Earth's mantle by influencing phase stability, density, and elastic properties, and helping to govern defect-mediated behavior including electrical and thermal conductivity and rheology. Since transition metals are also somewhat siderophile, geochemical measurements of absolute and relative abundances of transition metals in mantle-derived rocks help constrain the evolution of the core/mantle system, including initial segregation and continuing reactions. Understanding the transition metals' roles in deep Earth transport properties and interpreting the geochemical record in terms of partitioning of transition metals among oxide, silicate, and metal phases requires a suite of measurements at the high pressure and temperature conditions of the mantle, including their thermoelastic equation of states, phase stability, and partitioning behavior.

In particular, the partitioning of cobalt and nickel between reduced metallic core material and oxide/silicate phases has been measured and used to predict the conditions of an early core-mantle boundary (Bouhifd et al. 2011; Kegler et al. 2008; Li and Agee 1996, 2001; O'Neill et al. 1998; Righter 2003; Siebert et al. 2012; Tschauner et al. 1999). However, at pressures and temperatures corresponding to the lower mantle, partitioning measurements become increasingly difficult to make in ultrahigh pressure devices such as the diamond anvil cell due to the small sample sizes, large temperature gradients, and lack of control over the chemical environment, especially oxygen fugacity. An alternate path to predicting the redox tendencies of metal/oxide systems in the deepest part of the Earth's mantle is to measure the thermoelastic properties directly at the temperatures and pressures relevant to the Earth's mantle, and use these values to calculate relative free energies of redox reactions at extreme conditions (e.g. Campbell et al. 2009). While equation of state measurements exist for the Fe/FeO and Ni/NiO systems

(Campbell et al. 2009), the phase stability and equation of state of cobalt oxide has not been studied at simultaneous high pressure and temperature.

In addition, insulating solids containing transition metal oxides are used in a variety of applications that take advantage of their highly-correlated electron behaviors. Therefore, there has been some community effort to understand the behavior of transition metal oxides, including cobalt oxide, at high pressure. At ambient conditions cobalt oxide adopts a paramagnetic rock salt structure and like several other transition metal oxides it undergoes a slight combined rhombohedral and tetragonal distortion to an antiferromagnetic phase below its Néel temperature (Wdowik and Legut 2008; Roth 1958; Shull et al. 1951). The bulk modulus of the B1 phase of cobalt oxide has been measured both by ultrasonic (Sumino et al. 1980) and static (Guo et al. 2002) methods and its ambient pressure thermal expansion has been measured (Massobrio and Meyer 1991; Touzelin 1978). Cobalt oxide shows a pressure-induced distortion to the rhombohedral phase at 43 (2) GPa (Guo et al. 2002). At 90-97 GPa cobalt oxide undergoes a volume collapse that is associated with a high to low spin transition similar to ferropericlase (Guo et al. 2002; Rueff et al. 2005; Zhang et al. 2009).

To enrich our mineral physics understanding of transition metal oxide behavior at simultaneous high pressures and temperatures, and to assess the thermoelastic behavior of cobalt oxide, specifically in comparison with iron oxide and nickel oxide to infer relative transition metal compressibilities in the Earth's mantle, we measured the high pressure and high temperature phase stability and thermoelastic properties of cobalt oxide using the laser-heated diamond anvil cell in conjunction with synchrotron X-ray diffraction.

2. Experimental Methods

High pressure and temperature lattice parameter measurements of cobalt oxide were obtained at the GSECARS 13ID-D end-station at the Advanced Photon Source. The cobalt oxide sample material was a <5μm grain size powder loaded in a diamond anvil cell equipped with 200 μm-culet diamond and a rhenium gasket pre-compressed to a thickness of 20 μm, and drilled to a diameter of 90 μm. In the diamond cell sample chamber, the thin plate of cobalt oxide material was loaded between two ~8 μm plates of dry powdered NaCl, which functioned as pressure medium, thermal insulator, and pressure standard. Samples were heated using a double-sided fiber IR laser system that had a beam profile with a 15 μm flat top region and a full width at half max of 25 μm (Prakapenka et al. 2008). Multiple temperature measurements were obtained from each side of the sample using the emitted Planck radiation during each X-ray exposure, with good agreement on each side indicating symmetric insulation. We report the mean value of 2 to 12 temperature measurements along with their standard deviations, which are generally less than 5% indicating good temporal stability.

A total of twenty heating cycles were performed on a single sample between 6 and 65 GPa. X-ray diffraction patterns were obtained before, during, and after each heating cycle using the GSECARS CCD imaging system with an X-ray spot size of ~5x5 μm and wavelength of 0.3344 Å. Sample to detector distances were calibrated using a CeO_2 standard. Intensity vs. two-theta X-ray diffraction patterns were generated from the two-dimensional image using the software Fit2D (Hammersley et al. 1996). The coaxial alignment of X-ray volume and laser hotspot is crucial for interpretation of high-pressure, high-temperature diffraction data (Kavner and Panero, 2004). Alignment was confirmed before and after each heating cycle using the visible X-ray fluorescence of NaCl. The alignment was found to be consistent within 5 μm

before and after each heating cycle. Since this is smaller than the 15 μm flat top region, the measured temperatures should be representative of the true sample temperature.

Diffraction patterns were indexed, and individual *d*-spacings determined by a Gaussian fit to each diffraction peak (Figure 1). In each diffraction pattern, the lattice parameter of cobalt oxide was determined from the (111), (200), and (220) *d*-spacings. The corresponding lattice parameter of the NaCl B1 structure was determined using the (111), (200), (220), (311), (222), (400), and (420) peaks and the lattice parameter of the NaCl B2 structure was determined using the (100), (110), (111), (200), and (210) diffraction peaks. The positions of the diffraction peaks of cobalt oxide display significant azimuthal strain anisotropy at room temperature. However, upon heating, the anisotropy disappears (Figure 1). For this reason we omit our ambient temperature measurements from our determination of high pressure and temperature thermoelastic properties. For the patterns obtained during laser heating, we do not observe broadening or splitting of either the cobalt oxide (111) or (220) diffraction peak that would indicate a transition to the rhombohedral phase. Additionally there is no abrupt change in the goodness-of-fit to the cubic structure with increasing pressure. Therefore, we interpret all of our high temperature data in terms of the B1 structure of cobalt oxide.

The pressure corresponding to each high P, T diffraction pattern is determined by referencing the measured NaCl lattice parameter to the high pressure and temperature equation of state of NaCl. Because NaCl acts as a thermal insulator between the laser-heated samples and the diamonds, we assume that the average temperature of our NaCl pressure calibrant is halfway between the measured temperature at the sample and the temperature of the diamond (assumed to be ambient temperature) such that $T_{NaCl} = (T_{meas} + 300\ K)/2$. This assumption affects the accuracy of the pressure determination and therefore the determination of the equation of state.

For example, alternately assuming $T_{NaCl} = (3T_{meas} + 300K)/4$ (following Campbell et al. 2009) results in a 7% increase in the Grüneisen parameter and a 30% decrease in the *q* value. This decreases the predicted density of cobalt oxide by ~0.5% at pressures and temperatures of the lower mantle. Because NaCl undergoes a transformation to the B2 phase at ~30 GPa, a change in the reference state is necessary in the middle of the pressure range of our measurements. (Dorogokupets and Dewaele 2007; Fei et al., 2007). This introduces a dichotomy arising from differences between two separate groups of published equation of state parameters for NaCl B1 (Decker 1971 and Dorogokupets and Dewaele 2007) and NaCl B2 (Dorogokupets and Dewaele 2007 and Fei et al. 2007). While the Decker and Dorogokupets equations of state for B1 NaCl are in good agreement throughout our experimental range, the Fei B2 NaCl equation of state registers a pressure that is systematically lower than that of Dorogokupets and Dewaele by about 7%. As a result, using Fei's NaCl B2 standard introduced an apparent kink in the pressure-volume curve of cobalt oxide at the B1-B2 transition pressure. For this reason we use Dorogokupets and Dewaele's equation of state, which yields consistent results across the whole pressure range. Using this equation of state, in patterns that have both the B1 and B2 structures of NaCl present we find agreement between the inferred pressures within 1 GPa.

3. Results: Thermal equation of state of cobalt oxide

Appendix A lists the data used to determine the high pressure and temperature equation of state of cobalt oxide, including lattice parameters of CoO and NaCl, temperatures, and pressures inferred from the NaCl equation of state. The high pressure and temperature equation of state for B1-structured cobalt oxide is constructed using a reference isotherm with a thermal pressure correction following equation 1:

$$P(V,T) = P_{300K}(V) + P_{th}(V,T) \quad (1)$$

For the isothermal reference P(V) equation of state we use a Birch-Murnaghan formulation (Birch 1947) given as

$$P_{300K}(V) = \frac{3K_{0T}}{2}\left[\left(\frac{V_0}{V}\right)^{\frac{7}{3}} - \left(\frac{V_0}{V}\right)^{\frac{5}{3}}\right]\left[1 + \frac{3}{4}\left(K' - 4\right)\left(\left(\frac{V_0}{V}\right)^{\frac{2}{3}} - 1\right)\right] \quad (2)$$

where V_0 is the ambient pressure unit cell volume, K_{0T} is the ambient isothermal bulk modulus and K´ is its first pressure derivative, evaluated at P=0. We define the thermal pressure using the Mie-Grüneisen-Debye model given by

$$P_{th}(V,T) = \frac{\gamma}{V} 3nk\left[T\int_0^{\frac{\theta}{T}} \frac{z^3 dz}{\left(e^z - 1\right)} - 300K\int_0^{\frac{\theta}{300K}} \frac{z^3 dz}{\left(e^z - 1\right)}\right] \quad (3)$$

where γ is the Grüneisen parameter and scales as $\gamma(V) = \gamma_0\left(\frac{V}{V_0}\right)^q$, n is the number of atoms per formula unit, k is the Boltzmann constant, θ is the Debye temperature and varies as $\theta(V) = \theta_0 \exp\left[\frac{\gamma_0}{q}\left(1 - \left(\frac{V}{V_0}\right)^q\right)\right]$, and q is a unit-less scaling factor. To extend the V/V_0 range of our analysis we include an additional dataset comprising ambient pressure thermal expansion measurements by Touzelin (1978; via Massobrio and Meyer 1991). These measurements help constrain the parameter q while avoiding pressure calibration issues.

The entire high pressure, high temperature data set is fit to the above equations using a linear-least squares regression and fixing the values of V_0 to 77.4 Å^3 (Guo et al. 2002; Sumino et al. 1980) and θ_0=517.8 K (Freer 1981). Our best-fit parameters for the high P,T data set of B1 cobalt oxide are K_{0T}=190 (1) GPa, K'=3.49 (4), γ_0=1.54 (4), and q=2.87 (15) (Table 1; Figure

2a). Residuals between the predicted pressure from our equation of state and measured pressure are mostly within one standard deviation of zero and show no significant trends with pressure or temperature (Figure 2b).

Looking at the relative equation of state parameters for CoO, NiO, and FeO (Table 1) we notice several trends. Moving from left to right on the periodic table (Fe, Co, Ni) we see decreasing V_0 and increasing bulk modulus and Grüneisen parameter. These systematic differences in thermoelastic response directly lead to differing redox behavior at deep Earth conditions.

4. Discussion

4.1 High pressure free energy difference between cobalt oxide and cobalt metal

We use our newly constrained equation of state of cobalt oxide in conjunction with existing measurements of the high pressure/temperature equation of state of cobalt metal to calculate the free energy of the Co/CoO system at high pressures and temperatures. The Gibbs free energy of cobalt oxide can be calculated by referencing the ambient pressure and high temperature value $\Delta G_{1bar}(T)$ (Chase 1998 and Fredriksson and Seetharaman 2004) with an additional term for the work done on the sample by increasing pressure:

$$\Delta G(P,T_0) = \Delta G(1\ \text{bar}, T_0) + \int V(P,T_0)dP \qquad (4)$$

Using this equation, we calculate $\Delta G(P,T)$ for cobalt oxide using the V(P,T) measured in this study. We also calculate $\Delta G(P,T)$ for Fe and FeO and Ni and NiO using data from Campbell et al. 2009 and for cobalt metal as detailed below. The relevant equation of state parameters are shown in Table 1.

Of all of these phases, the high pressure and temperature thermoelastic properties of cobalt metal have the most uncertainty. At least three phases of cobalt have been observed at high pressures: ε-hcp, γ-fcc and β-fcc (Yoo et al 2000) and no simultaneous high pressure and temperature equation of state static compression data exists for any of these phases. The γ phase is likely the relevant phase at Earth's lower mantle conditions (Yoo et al. 2000) but lacks compressibility measurements. However, the Clapeyron slope between ε and γ cobalt is extremely shallow (Yoo et al. 2000) suggesting a small volume change across the phase boundary. Thus we calculate the oxygen fugacity buffer relative to the ε-hcp cobalt phase, which has independent measurements of bulk modulus (Fujihisa 1996), Debye temperature (Furukawa et al. 1982), and the Grüneisen parameter from shockwave measurements (McQueen and Marsh 1960). The value of *q* for Co metal is not well constrained by experiments, and we fix it at 1 for these calculations.

To calculate the free energy differences between the transition metal and oxide pairs at high pressure and temperature, we adapt the approach outlined by Campbell et al. (2009). For the oxidation reaction:

$$M + \frac{1}{2}O_2 = MO \qquad (5)$$

the activity of oxygen (fO_2) at which metal and oxide are in equilibrium is a function of the Gibbs free energy of the solid phases and temperature, and is defined as

$$\ln fO_2 = \frac{2}{RT}\left(\Delta G_{MO} - \Delta G_M\right) \qquad (6)$$

It bears mentioning that at high pressure the oxygen fugacity (fO_2) of a system ceases to have a physical interpretation. We can say definitively that there is not gaseous molecular oxygen at 1 bar in equilibrium with metal and oxide in the deep Earth. However, oxygen fugacity

is a convenient reference state for comparing the relative preference of different elements to occupy an oxidized or reduced state. Alternately we can plot these redox reactions as a function of difference in Gibbs free energy between metal and oxide or as a standard reduction potential (e.g. Kavner et al. 2007).

Figure 3 shows the relationship among oxygen fugacity, Gibbs free energy, and standard reduction potential for the Co/CoO, Ni/NiO, and Fe/FeO phase boundaries as a function of temperature and pressure along a reference adiabat with a foot temperature of 1600 K (Katsura et al. 2010), similar to lower mantle conditions. The equilibrium oxygen fugacity of all three of the metal/metal oxide pairs increases with increasing pressure and decreases with temperature. The net effect along a lower-mantle adiabat is an increase in the oxygen fugacity of each metal/oxide pair. The curves for the Co/CoO phase boundary and the Ni/NiO phase boundary lie above the Fe/FeO boundary at all pressures on this plot. This means that throughout lower mantle conditions, iron will preferentially oxidize over both cobalt and nickel. At low pressure the Co/CoO curve is lower than Ni/NiO, but crosses and becomes higher at ~58 GPa. This suggests that at low pressure cobalt will preferentially oxidize over nickel, but at high pressure the reverse is true.

To more closely examine the relative redox behavior of cobalt and nickel we plot the Gibbs free energy of the reaction Co+NiO=CoO+Ni as a function of pressure and temperature (Figure 4). The black line in Figure 4 defines a pressure-temperature trajectory along which the free energy of the reaction is zero. On the left side of this plot, at lower pressures, this reaction proceeds forward, stabilizing CoO and Ni with respect to Co metal and NiO. But at high pressures, the reaction reverses, resulting in oxidation of Ni to NiO and reduction of CoO to Co metal. This result predicts a mid-mantle crossing point in the relative siderophility of Ni and Co.

In the next paragraph we examine the major sources of systematic uncertainties in this crossing point determination. In the next section we elucidate some of the implications for predicting relative partition coefficients of Co and Ni in the deep mantle, predictions of Co and Ni content as a function of depth in the mantle, and for understanding chemical signatures of core-mantle segregation.

These plots rely on our calculation of the free energy difference between cobalt oxide and cobalt metal at high pressures and temperatures. Our three major sources of systematic uncertainties for this calculation are: (1) Error in the cobalt oxide equation of state arising from errors in temperature determination, as discussed above; (2) Uncertainty arising from uncertainties in the relevant cobalt metal equation of state; and (3) systematic errors arising from comparing the thermoelastic behavior of materials that have been calibrated using different standards. Each of these sources of error generate uncertainty in the exact pressure and temperature of the crossover between the nickel oxide and cobalt oxide systems, but unless extreme, they will not alter the fact that a crossover exists at approximately mid-mantle pressures, which is our bottom line result. We tested the sensitivity of the free energy contour plot (Fig. 4) to ± 10% perturbations in the equation of state parameters of cobalt metal. These result in some changes in the topography of the free-energy difference plot (shown in the Supplementary materials) but always show a crossing point of the NiO/Ni and Co/CoO systems at approximately mid-mantle pressures and temperatures.

4.2 Metal-oxide partitioning in the deep Earth

We are particularly interested in the pressure and temperature conditions of the crossing point shown in Figure 4 since the Earth's mantle is observed to be about equally depleted in

nickel and cobalt (Righter 2003), and the above relation defines a point at which both are equally likely to be partitioned into an iron-rich core. There are several pieces of information that can be extracted from this figure. The first is an approximate pressure at which the partitioning of cobalt and nickel between oxidized and reduced phases is consistent with observations of their mantle depletions. This pressure can be interpreted as the pressure of the core mantle boundary during core mantle equilibration. This is assuming that exchange of siderophile elements between metallic and oxidized phases occurs only at this boundary, and that the mantle is convecting rapidly enough to stay well mixed. Alternately we can imagine a scenario in which descending droplets of metal equilibrate with the surrounding mantle until they reach the core. In this case the equilibrium pressure would be closer to the midpoint in the magma ocean column. Another piece of information we can extract from Figure 4 is the temperature dependence of the equilibrium point. The slope of the equilibrium contour in Figure 4 above 1800 K is ~80 K/GPa. This suggests that hotter models of the early Earth will increase the depth at which the appropriate depletion is achieved.

The free energies of these redox reactions can be used in a simplified model to make quantitative predictions about the partitioning of cobalt and nickel between oxidized and reduced phases. The calculation in the previous section makes several predictions about the behavior of cobalt and nickel in the early Earth. However, we are unsure about whether considering free energy alone is sufficient to explain the partitioning behavior of these elements. To test this we calculate partition coefficients, and compare them to direct measurements of element partitioning. While the exact nature of the phase and partitioning behavior will depend on the ternary Ni-Co-O phase diagram, we can make predictions if we assume that the Ni-Co metal phases show complete solid solution (as suggested by Guillermet 1989) and the NiO-CoO rock

salt oxide phases show complete solid solution. We can do this by directly appealing to partition coefficients. Following Campbell et al. (2009), for a system with an oxide phase in equilibrium with a metallic phase, we can define a partition coefficient for species M (assumed here to be either Ni or Co, and with a +2 oxidation state in the oxide) between a metal and oxide phase $D_M^{metal/oxide}$:

$$D_M^{metal/oxide} = \frac{X_M^{metal}}{X_{MO}^{oxide}} = \left(\frac{\gamma_{MO}^{oxide}}{\gamma_{Ml}^{metal}}\right)(fO_2)^{\frac{-1}{2}} \exp\left(\frac{\Delta G_{MO} - \Delta G_M}{RT}\right) \quad (7)$$

where X_M^{metal} and X_{MO}^{oxide} are the concentration of element M in the metal and oxide phase respectively, and γ denotes the activity coefficient of the M species within each phase. Here we make the simplifying assumption that the activity coefficients are unity (Raoult's law). In this case the partitioning of an element between metallic and oxide phases depends solely on the Gibbs free energy of each phase, the temperature, and the absolute oxygen fugacity of the system. To simplify the comparison of results obtained between experiments with variable oxygen fugacity partition coefficients are often normalized by a second element (commonly iron) to form an exchange coefficient, which is independent of oxygen fugacity.

$$K_{D_{M/Fe}^{metal/oxide}} = \frac{D_M^{metal/oxide}}{D_{Fe}^{metal/oxide}} = \frac{\frac{X_M^{metal}}{X_{MO}^{oxide}}}{\frac{X_{Fe}^{metal}}{X_{FeO}^{oxide}}} = \frac{\frac{\gamma_{MO}^{oxide}}{\gamma_M^{metal}}}{\frac{\gamma_{FeO}^{oxide}}{\gamma_{Fe}^{metal}}} \exp\left(\frac{\Delta G_{MO} + \Delta G_{Fe} - \Delta G_M - \Delta G_{FeO}}{RT}\right) \quad (8)$$

Equivalently, this can be thought of as looking at the equilibrium constant of the redox reaction: $Fe + MO = M + FeO$.

A high value of K_D indicates that the reaction will proceed strongly to the right, a low value, to the left. Figure 5 shows calculated exchange coefficients for cobalt and nickel between metal and oxide phases as a function of pressure along a 2473 K isotherm. This isotherm is

chosen to facilitate comparison with metal/oxide partitioning measurements at the same temperature by O'Neill et al. (1998). Both our predictions and O'Neill's data show that the Co/CoO and Ni/NiO curves cross each other at high pressure, at ~61 GPa for our predictions, and ~40 GPa for O'Neill's measurements. Therefore, our simplified model predicts the measured relative partitioning behavior of the Ni/NiO and Co/CoO systems. In detail, compared to O'Neill's measured values we predict higher intercepts and shallower slopes for both nickel and cobalt. There are several possible explanations for the differences. Non-unity activity coefficients and the mixing entropy of the solid solution are both unaccounted for by our model. Additionally, we are comparing our predictions of solid/solid equilibrium to measurements in a wholly molten system. As a result, there should be an additional term for the free energy difference between solid and liquid:

$$K_D = \frac{\frac{\gamma_{MO}^{oxide}}{\gamma_{M}^{metal}}}{\frac{\gamma_{FeO}^{oxide}}{\gamma_{Fe}^{metal}}} \exp\left(\frac{\Delta G_{MO} + \Delta G_{Fe} - \Delta G_{M} - \Delta G_{FeO}}{RT} + \frac{\Delta G_{MMO}^{liq} - \Delta G_{MMO}^{sol} + \Delta G_{FeFeO}^{liq} - \Delta G_{FeFeO}^{sol}}{RT} \right) \quad (9)$$

We make the implicit assumption that the solid/liquid free energy difference for nickel and cobalt is exactly offset by the difference for iron, but this may not be the case. In the case of activities that are lower than predicted by Raoult's law we would expect steeper pressure slopes than are plotted in Figure 5.

Although our model is designed to examine partitioning trends between metals and their oxides, experimental observations of partitioning between metal and silicates show similar trends. For example measurements of the partitioning behavior of Ni and Co between metal and silicate systems (Bouhifd et al. 2011; Kegler et al. 2008; Li and Agee 1996, 2001; Siebert et al. 2012; Tschauner et al. 1999) demonstrate increasing siderophile behavior of cobalt with respect

to nickel at high pressures, although the quantitative partitioning behavior is sensitive to the details of the silicate and metal compositions. This qualitative agreement of pressure-dependent partitioning trends for cobalt and nickel between reduced metal and a variety of oxidized phases suggest that to first order, the elemental partitioning is governed not by the identity of the oxidized phase, but by the order of the metal/metal oxide system in a reactivity series, analogous to an electrochemical series or a table of standard reduction potentials, that may depend on pressure and temperature.

4.3 Towards a Deep-Earth Electrochemical Series

In analogy with an aqueous table of standard reduction potentials (e.g. Milazzo et al. 1978), in which relative tendency of one species to oxidize or reduce is quantified for aqueous systems at ambient pressures and temperatures, we hypothesize that a metal/metal oxide series can be constructed for temperatures and pressures throughout the Earth's mantle from thermodynamic data and equation of state data. Based on the measurements presented here, we interpret Figure 3 as a determination of the electrochemical series of the Fe, Ni, and Co systems throughout the mantle. Although Figure 3 and our partitioning calculations are based on metal/metal oxide systems, the general agreement in predicting a crossover in cobalt and nickel partitioning behavior across different systems suggests that the relative standard reduction potentials of these elements with respect to iron are mostly independent of the details of their speciation in the oxide or silicate phase. Therefore, when considering questions of elemental partitioning between metallic and oxidized phases in Earth and planets, the relative standard reduction potentials, calculated at the relevant pressure and temperature, will be the first-order determinant of which elements preferentially partition into the core and which remain in the

mantle phases. A high pressure/temperature electrochemical series can be used to address a variety of different questions about how to interpret geochemical signatures in terms of early core-mantle segregation and/or reactions across the current core-mantle boundary.

Acknowledgements

This work was supported by a grant from DOE/NNSA to the Carnegie/DOE Alliance Center and by the NSF under grant number EAR 0510914 and EAR 969033. Portions of this work were performed at GeoSoilEnviroCARS (Sector 13), Advanced Photon Source (APS), Argonne National Laboratory. GeoSoilEnviroCARS is supported by the National Science Foundation - Earth Sciences (EAR-1128799) and Department of Energy - Geosciences (DE-FG02-94ER14466). Use of the APS was supported by the U. S. Department of Energy, Office of Science, Office of Basic Energy Sciences, under Contract No. DE-AC02-06CH11357. We thank Dr. Matthew Whitaker and an anonymous reviewer for their detailed and constructive reviews.

References

Birch, F. (1947) Finite elastic strain of cubic crystals. Physical Review, 71, 809-824.

Bouhifd, M. A. and Jephcoat, A. P. (2011) Convergence of Ni and Co metal-silicate partition coefficients in the deep magma-ocean and coupled silicon-oxygen solubility in iron melts at high pressures. Earth and Planetary Science Letters, 307, 341-348

Brown, J. M. and Shankland, T. J. (1981) Thermodynamic parameters in the Earth as determined from seismic profiles. Geophysical Journal of the Royal Astronomical Society, 66, 579-596

Campbell, A. J., Danielson, L., Righter, K., Seagle, C. T., Wang, Y. B., and Prakapenka, V. B. (2009) High pressure effects on the iron-iron oxide and nickel-nickel oxide oxygen fugacity buffers. Earth and Planetary Science Letters, 286, 556-564

Chase Jr., M.W., (1998) NIST-JANAF Thermochemical Tables, 4th ed. : Journal of Physical and Chemical Reference Data Monograph No. 9. American Institute of Physics.

Decker, D. L. (1971) High-pressure equation of state for NaCl, KCl, and CsCl. Journal of Applied Physics Physics, 42, 3239-3244

Dewaele, A., Loubeyre, P., Occelli, F., Mezouar, M., Dorogokupets, P. I., and Torrent, M. (2006) Quasihydrostatic equation of state of iron above 2 Mbar. Physical Review Letters, 97, 215504

Dorogokupets, P. I. and Dewaele, A. (2007) Equations of state of MgO, Au, Pt, NaCl-B1, and NaCl-B2: Internally consistent high-temperature pressure scales. High Pressure Research, 27, 431-446

Fei, Y., Ricolleau, A., Frank, M., Mibe, K., Shen, G., and Prakapenka, V. (2007) Toward an internally consistent pressure scale. Proceedings of the National Academy of Sciences, 104, 9182-9186

Fredriksson, P. and Seetharaman, S. (2004) On the standard Gibbs energy of formation of CoO. Scandinavian Journal of Metallurgy, 33, 305-309

Freer, R. (1981) Debye temperatures of oxides with the NaCl structure. Journal of Materials Science, 16, 3225-3227

Fujihisa, H. and Takemura, K. (1996) Equation of state of cobalt up to 79 GPa. Physical Review B, 54, 5-7

Furukawa, G. T., Douglas, T. B., and Pearlman, N. (1982) Heat Capacities, in: Zemansky, M. W., Gray, D. E. (Eds.), American Institute of Physics Handbook: Third Edition. McGraw-Hill., New York, pp. 4-115.

Guillermet, F. A. (1989) Assessing the thermodynamics of the Fe-Co-Ni system using a CAPHAD predictive technique. CALPHAD, 13, 1-22

Guo, Q., Mao, H. K., Hu, J., Shu, J., and Hemley, R. J. (2002) The phase transitions of CoO under static pressure to 104 GPa. Journal of Physics: Condensed Matter, 14, 11369-11374

Hammersley, A. P., Svensson, S. O., Hanfland, M., Fitch, A. N., and Hausermann, D. (1996) Two-dimensional detector software: From real detector to idealized image or two-theta scan. High Pressure Research, 14, 235-248

Katsura, T., Yoneda, A., Yamazaki, D., Yoshino, T., and Ito, E. (2010) Adiabatic temperature profile in the mantle. Physics of the Earth and Planetary Interiors, 183, 212-218

Kavner, A. and Panero, W., (2004) Temperature gradients and evaluation of thermoelastic properties in the synchrotron-based laser-heated diamond cell. Physics of the Earth and Planetary Interiors, 143-144, 527-539

Kavner, A., Walker, D., Sutton, S., and Newville, M (2007) Externally-driven charge transfer in silicates at high pressure and temperature: A XANES study. Earth and Planetary Science Letters, 256, 314-327

Kegler, P., Holzheid, A., Frost, D. J., Rubie, D. C., Dohmen, R., and Palme, H. (2008) New Ni and Co metal-silicate partitioning data and their relevance for an early terrestrial magma ocean. Earth and Planetary Science Letters, 268, 28-40

Li, J. and Agee, C. B. (1996) Geochemistry of mantle-core differentiation at high pressure. Nature, 381, 686-689

Li, J. and Agee, C. B. (2001) The effect of pressure, temperature, oxygen fugacity and composition on partitioning of nickel and cobalt between liquid Fe-Ni-S alloy and liquid silicate: Implications for the Earth's core formation. Geochimica et Cosmochimica Acta, 65, 1821-1832

Massobrio, C. and Meyer, M. (1991) Rigid-ion models for NiO and CoO: comparison between experimental and calculated thermal expansion. Journal of Physics: Condensed Matter, 3, 279-284

McQueen, R. G. and Marsh, S. P. (1960) Equation of state for nineteen elements from shock-wave measurements to two Megabars. Journal of Applied Physics, 31, 1253-1269

Milazzo, G., Caroli, S., and Braun, R. D. (1978) Tables of Standard Electrode Potentials, Journal of the Electrochemical Society, 125(6), 261C

Murakami, M., Hirose, K., Ono, S., Tsuchiya, T., Isshiki, M., and Watanuki, T. (2004) High pressure and high temperature phase transitions of FeO. Physics of the Earth and Planetary Interiors, 146, 273-282

O'Neill, H. S. C., Canil, D., and Rubie, D. C. (1998) Oxide-metal equilibria to 2500°C and 25 GPa: Implications for core formation and the light component in the Earth's core. Journal of Geophysical Research, 103, 12239-12260

Prakapenka, V. B., Kubo, A., Kuznetsov, A., Laskin, A., Shkurikhin, O., Dera, P., Rivers, M. L., and Sutton S. R. (2008) Advanced flat top laser heating system for high pressure research at GSECARS: application to the melting behavior of germanium. High Pressure Research, 28, 225-235

Righter, K. (2003) Metal-silicate partitioning of siderophile elements and core-formation in the Early Earth. Annual Review of Earth and Planetary Science, 31, 135-174

Roth, W. L. (1958) Magnetic structures of MnO, FeO, CoO, and NiO. Physical Review, 110, 1333-1341

Rueff, J. P., Mattila, A., Badro, J., Vankó, G. and Shukla., A., (2005) Electronic properties of transition-metal oxides under high pressure revealed by x-ray emission spectroscopy. Journal of Physics: Condensed Matter, 17, S717-S726

Shull, C. G., Strauser, W. A., and Wollan, E. O. (1951) Neutron diffraction by paramagnetic and antiferromagnetic substances. Physical Review, 83, 333-345

Siebert, J., Badro, J., Antonangeli, D., and Ryerson, F. J. (2012) Metal-Silicate partitioning of Ni and Co in a deep magma ocean. Earth and Planetary Science Letters, 321-322, 189-197

Sumino, Y., Kumazawa, M., Nishizawa, O., and Pluschkell, W. (1980) The elastic constants of single crystal $Fe_{1-x}O$, MnO, and CoO, and the elasticity of stoichiometric magnesiowüstite. Journal of Physics of the Earth, 28, 475-495

Touzelin, B. (1978) Study by high-temperature X-ray diffraction under controlled atmosphere of cobalt and nickel oxides. Revue Internationale des Hautes Temperatures et des Réfractaires 15, 33-41

Tschauner, O., Zerr, A., Specht, S., Rocholl, A., Boehler, R., Palme, H. (1999) Partitioning of nickel and cobalt between silicate perovskite and metal at pressures up to 80 GPa. Nature, 398, 604-607

Wdowik U. D. and Legut, D. (2008) CoO under pressure from first principles. Journal of Physics and Chemistry of Solids, 69, 1698-1703

Yoo, C. S., Cynn, H., Söderlind, P., and Iota, V. (2000) New β(fcc)-Cobalt to 210 GPa. Physical Review Letters, 84, 4132-4135

Zhang, W., Koepernik, K., Richter, M., and Eschrig, H. (2009) Magnetic phase transition in CoO under high pressure: A challenge for LSDA+U. Physical Review B, 79, 155123

Figure 1. Representative caked diffraction patterns. Diffraction peaks for cobalt oxide (C), NaCl B1 (B1), and NaCl B2 (B2) are labeled. **(upper)** Pattern obtained at 27 GPa at room temperature after laser heating. The cobalt oxide peaks show significant strain anisotropy. **(lower)** Pattern obtained at 30 GPa and ~2400 K. Strain anisotropy is not observed during heating.

Figure 2. **(a.)** Measured cobalt oxide unit cell volume as a function of pressure and (binned) temperature. Data using the NaCl B1 pressure calibrant (circles), NaCl B2 pressure calibrant (squares) and ambient pressure thermal expansion data from Touzelin 1978 (diamonds) are plotted. Uncertainties are within the size of the symbols. Isotherms constructed from the best-fit thermoelastic properties and at the lower bound of each temperature bin are drawn. **(b.)** Pressure residuals from (a). Error bars show 1σ uncertainties.

Figure 3. The oxygen fugacity (left axis), Gibbs free energy in kJ/mol (interior right axis), and standard reduction potential in volts(exterior right axis) of the Co/CoO, Ni/NiO, and Fe/FeO metal/oxide systems. The equilibria are calculated as a function of pressure along an adiabat with a foot temperature of ~1600 K (Katsura et al. 2010).

Figure 4. A plot of the Gibbs free energy change in kJ/mol for the reaction Co+NiO=CoO+Ni. At high pressures cobalt metal and nickel oxide is favored. At low pressures the reverse is true. Along the zero contour the reaction is balanced. The adiabat from Figure 3 is plotted in red and we can see the crossing point at ~58 GPa and ~2200 K. A kink in the plot is visible at 1800 K; this originates in the 1 bar ΔG values from Chase (1998).

Figure 5. Metal/oxide exchange coefficients as a function of pressure calculated for Ni/Fe (solid green line) and Co/Fe (solid blue line). All calculations are performed at 2473 K. Measured metal/oxide exchange coefficients for Co/Fe (circles) and Ni/Fe (squares) are plotted for comparison (O'Neill et al. 1998). The pressure trends of these measurements are plotted as dashed lines

Supplementary Figure 1a. Similar to Figure 4 in the text, but calculated assuming Co metal is more 10% more compressible (K_{0T}=179 GPa). The crossing point with the geotherm lowers by ~10% (to ~53 GPa from ~58 GPa).

Supplementary Figure 1b Similar to Figure 4, but assuming Co metal is 10% less compressible (K_{0T}=219 GPa). The crossing point with the geotherm moves to higher pressures and exhibits a double crossing behavior (at 77 and 85 GPa).

Table 1. Equation of state parameters used in the calculation of oxygen fugacity buffers.

Phase	V_0 (cm^3/mol)	K_T (GPa)	K′	θ_0 (K)	γ_0	q	Source
B1 CoO	11.653 (fixed)	190 (1)	3.49 (4)	517.8 (fixed)	1.54 (4)	2.87 (15)	This study
B1 CoO	11.653	180	3.82				Guo et al. 2002
B1 CoO	11.631	186 (5) (K_S)					Sumino et al. 1980
Co (hcp)	6.624	199	3.6				Yoo et al. 2000
Co					1.97		McQueen and Marsh 1960
Co				445			Furukawa et al. 1982
B1 NiO	10.973	190 (3)	5.4 (2)	480	1.80 (4)	1 (fixed)	Campbell et al. 2009
Ni (fcc)	6.587	179 (3)	4.3 (2)	415	2.50 (6)	1 (fixed)	Campbell

							et al. 2009
B1 FeO	12.256	146.9 (1.3)	4 (fixed)	380	1.42 (4)	1.3 (3)	Campbell et al. 2009
Fe (fcc)	7.076	133 (3)	5 (fixed)	470	1.95 (4)	1.6 (6)	Campbell et al. 2009
Fe (hcp)*	6.765	165	4.97	417	1.875	3.29	Dewaele 2006

*The equation of state of hcp iron incorporates additional anharmonic and electronic terms not described here.

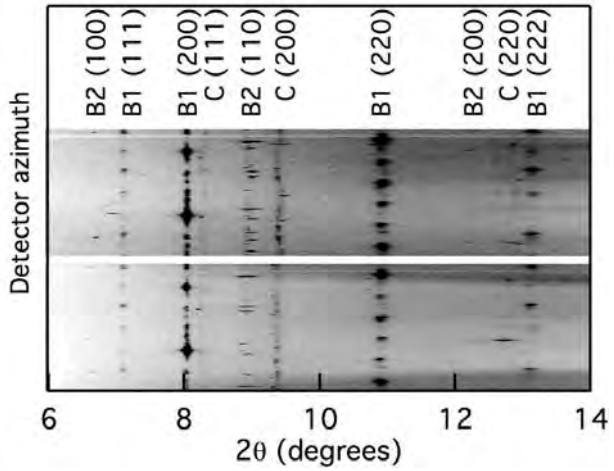

Figure 1. Representative caked diffraction patterns. Diffraction peaks for cobalt oxide (C), NaCl B1 (B1), and NaCl B2 (B2) are labeled. **(upper)** Pattern obtained at 27 GPa at room temperature after laser heating. The cobalt oxide peaks show significant strain anisotropy. **(lower)** Pattern obtained at 30 GPa and ~2400 K. Strain anisotropy is not observed during heating.

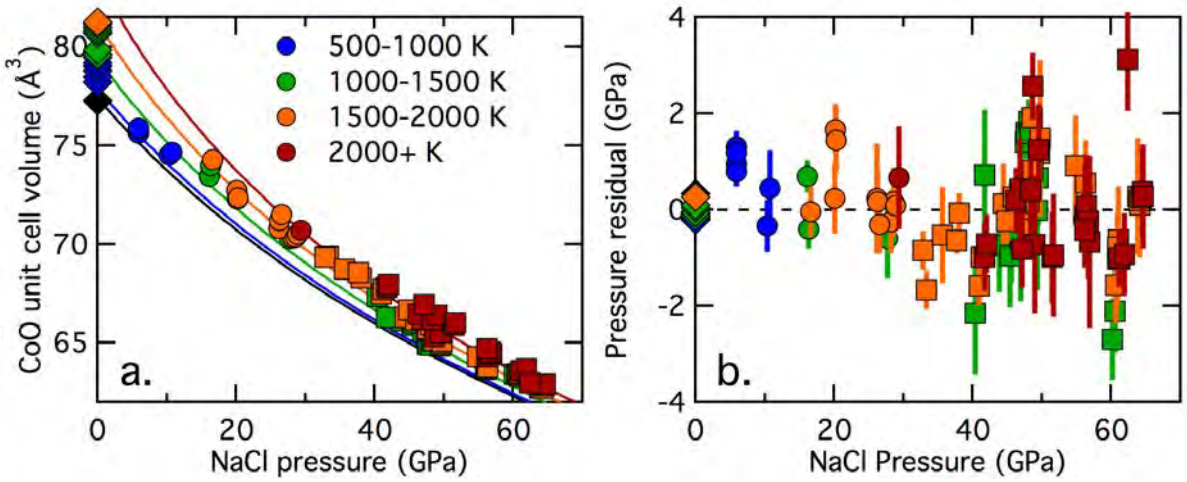

Figure 2. **(a.)** Measured cobalt oxide unit cell volume as a function of pressure and (binned) temperature. Data using the NaCl B1 pressure calibrant (circles), NaCl B2 pressure calibrant (squares) and ambient pressure thermal expansion data from Touzelin 1978 (diamonds) are plotted. Uncertainties are within the size of the symbols. Isotherms constructed from the best-fit thermoelastic properties and at the lower bound of each temperature bin are drawn. **(b.)** Pressure residuals from (a). Error bars show 1σ uncertainties.

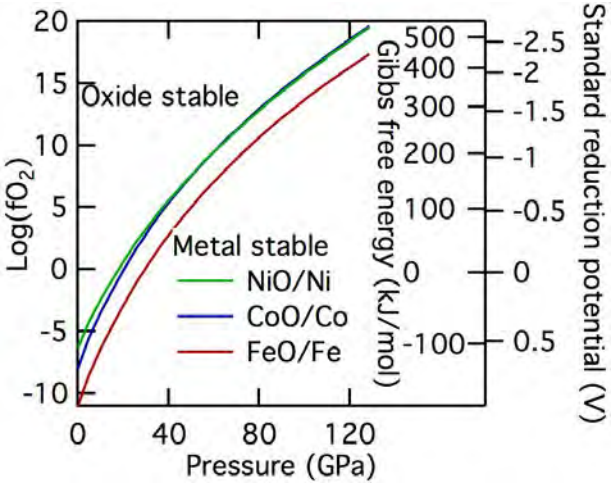

Figure 3. The oxygen fugacity (left axis), Gibbs free energy in kJ/mol (interior right axis), and standard reduction potential in volts(exterior right axis) of the Co/CoO, Ni/NiO, and Fe/FeO metal/oxide systems. The equilibria are calculated as a function of pressure along an adiabat with a foot temperature of ~1600 K (Katsura et al. 2010).

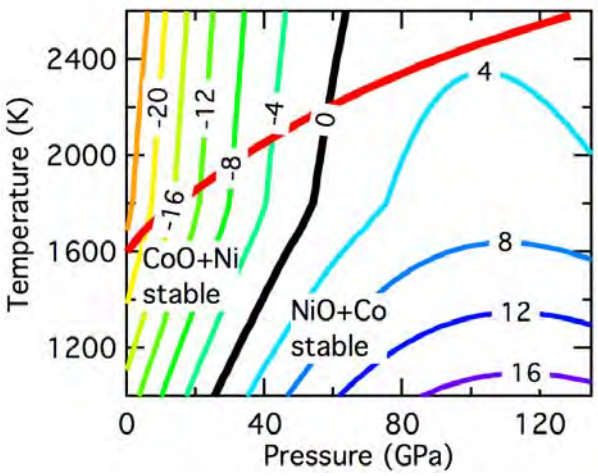

Figure 4. A plot of the Gibbs free energy change in kJ/mol for the reaction Co+NiO=CoO+Ni. At high pressures cobalt metal and nickel oxide is favored. At low pressures the reverse is true. Along the zero contour the reaction is balanced. The adiabat from Figure 3 is plotted in red and we can see the crossing point at ~58 GPa and ~2200 K. A kink in the plot is visible at 1800 K; this originates in the 1 bar ΔG values from Chase (1998).

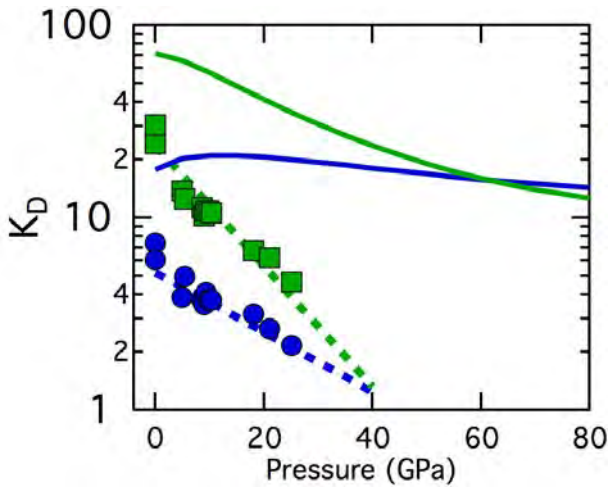

Figure 5. Metal/oxide exchange coefficients as a function of pressure calculated for Ni/Fe (solid green line) and Co/Fe (solid blue line). All calculations are performed at 2473 K. Measured metal/oxide exchange coefficients for Co/Fe (circles) and Ni/Fe (squares) are plotted for comparison (O'Neill et al. 1998). The pressure trends of these measurements are plotted as dashed lines.

Supplemental Materials

Measured unit cell volumes for sample and standard, average measured temperatures, and inferred pressures from the NaCl standard. NaCl unit cell volumes are the B2 structure unless otherwise indicated (* =B1)

.

file	NaCl Volume ($Å^3$)	Uncertainty ($Å^3$)	NaCl P (GPa)	Uncertainty (GPa)	CoO V ($Å^3$)	Uncertainty ($Å^3$)	Sample Temperature (K)	Uncertainty (K)
DAC_I_060*	154.633	0.220	5.91	0.07	75.887	0.042	832	7
DAC_I_061*	154.288	0.266	5.91	0.10	75.862	0.049	759	37
DAC_I_062*	154.223	0.517	5.92	0.18	75.652	0.048	754	39
DAC_I_063*	154.031	0.443	5.90	0.14	75.659	0.150	695	16
DAC_I_067*	142.355	0.276	10.36	0.16	74.510	0.114	700	64
DAC_I_068*	142.355	0.291	10.76	0.23	74.657	0.087	963	118
DAC_I_080*	133.487	0.287	16.12	0.20	73.445	0.029	1321	42
DAC_I_081*	133.622	0.528	16.58	0.36	74.281	0.020	1672	63

DAC_I_082*	133.480	0.476	16.27	0.32	73.968	0.021	1416	40
DAC_I_093*	128.158	0.357	20.26	0.30	72.358	0.142	1597	59
DAC_I_094*	128.190	0.408	20.21	0.33	72.279	0.086	1581	48
DAC_I_097*	128.264	0.447	20.12	0.37	72.728	0.139	1560	72
DAC_I_103*	121.224	0.347	26.15	0.47	70.817	0.052	1534	183
DAC_I_105*	121.513	0.400	26.28	0.42	71.215	0.105	1783	70
DAC_I_106*	121.450	0.335	26.57	0.36	71.502	0.078	1920	67
DAC_I_113*	119.355	0.394	27.71	0.46	70.305	0.109	1340	99
DAC_I_114*	119.188	0.436	28.17	0.48	70.341	0.095	1510	40
DAC_I_115*	119.050	0.323	28.62	0.36	70.374	0.141	1692	41
DAC_I_116*	118.998	0.289	28.84	0.32	70.490	0.102	1791	20
DAC_I_117*	119.023	0.179	29.35	0.22	70.693	0.256	2111	53
DAC_I_123	27.825	0.002	33.31	0.04	69.395	0.090	1562	22
DAC_I_124	27.927	0.028	32.79	0.16	69.340	0.081	1578	22
DAC_I_133	27.464	0.008	35.67	0.20	68.724	0.181	1738	105

DAC_I_143	27.212	0.010	37.63	0.10	68.580	0.033	1983	38
DAC_I_144	27.136	0.026	38.06	0.19	68.302	0.058	1965	49
DAC_I_154	26.556	0.039	40.35	0.28	67.348	0.258	1234	21
DAC_I_155	26.569	0.035	40.97	0.27	67.495	0.041	1595	52
DAC_I_156	26.635	0.033	41.18	0.25	67.710	0.044	1930	54
DAC_I_157	26.608	0.038	41.73	0.28	67.815	0.128	2121	48
DAC_I_158	26.627	0.038	42.01	0.29	67.944	0.097	2329	56
DAC_I_162	26.328	0.025	41.69	0.18	66.289	0.260	1127	1
DAC_I_171	26.018	0.029	43.84	0.23	66.121	0.175	1108	34
DAC_I_172	26.071	0.027	44.38	0.21	66.302	0.155	1569	21
DAC_I_173	26.104	0.024	44.87	0.20	66.679	0.075	1938	42
DAC_I_183	25.819	0.042	45.42	0.33	65.884	0.191	1159	6
DAC_I_184	25.878	0.034	45.54	0.28	66.042	0.188	1441	47
DAC_I_185	25.928	0.034	45.84	0.27	66.178	0.040	1780	29
DAC_I_186	25.960	0.025	46.26	0.21	66.460	0.122	2112	38

DAC_I_189	25.945	0.028	47.15	0.24	66.935	0.143	2500	57
DAC_I_193	25.635	0.050	46.89	0.41	65.556	0.212	1197	10
DAC_I_194	25.661	0.046	47.39	0.38	65.651	0.099	1542	36
DAC_I_195	25.672	0.055	47.59	0.46	65.732	0.078	1686	51
DAC_I_196	25.685	0.052	48.11	0.46	65.933	0.042	1994	88
DAC_I_197	25.868	0.003	46.83	0.18	66.214	0.185	2050	89
DAC_I_198	25.690	0.060	48.92	0.53	66.407	0.239	2417	99
DAC_I_199	25.738	0.073	48.34	0.60	66.174	0.127	2314	67
DAC_I_207	25.497	0.032	48.11	0.30	64.867	0.031	1265	65
DAC_I_208	25.525	0.034	47.58	0.29	64.914	0.016	1110	35
DAC_I_209	25.546	0.031	47.67	0.26	64.973	0.036	1238	17
DAC_I_210	25.533	0.046	48.30	0.39	65.098	0.025	1498	33
DAC_I_211	25.535	0.052	48.60	0.44	65.120	0.050	1656	11
DAC_I_212	25.547	0.050	48.67	0.42	65.413	0.110	1736	32
DAC_I_213	25.615	0.070	48.69	0.59	65.317	0.048	2012	56

DAC_I_214	25.534	0.058	49.49	0.50	65.507	0.140	2093	59
DAC_I_223	25.299	0.040	49.36	0.35	64.827	0.283	1096	4
DAC_I_224	25.347	0.043	49.43	0.37	64.891	0.164	1323	7
DAC_I_225	25.382	0.058	49.64	0.50	64.975	0.064	1565	39
DAC_I_226	25.417	0.047	49.72	0.40	65.064	0.279	1743	24
DAC_I_229	25.368	0.047	51.50	0.40	65.900	0.162	2424	3
DAC_I_230	25.386	0.055	51.67	0.48	66.026	0.216	2583	57
DAC_I_238	24.552	0.039	56.04	0.39	63.648	0.081	1181	4
DAC_I_240	24.578	0.041	56.13	0.40	63.743	0.056	1342	11
DAC_I_242	24.605	0.037	56.28	0.37	63.778	0.129	1530	41
DAC_I_244	24.709	0.053	56.38	0.51	64.291	0.155	2038	18
DAC_I_245	24.721	0.061	56.21	0.59	64.340	0.142	2005	62
DAC_I_248	24.681	0.072	56.88	0.70	64.448	0.278	2153	48
DAC_I_249	24.801	0.012	56.22	0.14	64.724	0.129	2358	39
DAC_I_250	24.738	0.004	56.71	0.05	64.549	0.206	2321	18

DAC_I_252	24.847	0.081	54.88	0.79	64.305	0.080	1908	107
DAC_I_261	24.136	0.051	60.13	0.53	63.420	0.103	1228	21
DAC_I_262	24.143	0.050	60.55	0.53	63.425	0.105	1461	37
DAC_I_263	24.160	0.038	60.60	0.40	63.399	0.108	1559	24
DAC_I_264	24.199	0.045	60.91	0.47	63.469	0.070	1888	22
DAC_I_265	24.193	0.047	61.20	0.50	63.553	0.059	1999	28
DAC_I_266	24.207	0.047	61.08	0.49	63.577	0.057	2006	1
DAC_I_267	24.196	0.045	61.88	0.47	63.693	0.111	2333	46
DAC_I_269	24.177	0.042	61.06	0.44	63.389	0.163	1859	6
DAC_I_270	24.142	0.041	60.93	0.43	63.299	0.141	1629	17
DAC_I_281	23.900	0.052	63.83	0.57	62.713	0.159	1837	37
DAC_I_282	23.894	0.052	64.02	0.59	62.738	0.131	1893	65
DAC_I_283	23.873	0.058	64.26	0.64	62.697	0.101	1908	39
DAC_I_284	23.883	0.056	64.12	0.62	62.737	0.134	1891	27
DAC_I_285	23.911	0.055	64.49	0.62	62.862	0.090	2197	61

DAC_I_286	23.913	0.064	64.55	0.71	62.898	0.122	2234	44
DAC_I_287	24.176	0.037	62.42	0.48	62.978	0.119	2494	128
Touzelin (1978)	-	-	-	-	77.260	0.014	299	5
Touzelin (1978)	-	-	-	-	78.205	0.014	589	5
Touzelin (1978)	-	-	-	-	78.480	0.014	683	5
Touzelin (1978)	-	-	-	-	78.788	0.014	774	5
Touzelin (1978)	-	-	-	-	79.036	0.014	852	5
Touzelin (1978)	-	-	-	-	79.202	0.014	911	5
Touzelin	-	-	-	-	79.457	0.014	980	5

(1978)								
Touzelin (1978)	-	-	-	-	79.596	0.014	1039	5
Touzelin (1978)	-	-	-	-	79.851	0.014	1117	5
Touzelin (1978)	-	-	-	-	80.672	0.014	1326	5
Touzelin (1978)	-	-	-	-	80.818	0.014	1375	5
Touzelin (1978)	-	-	-	-	80.980	0.014	1427	5
Touzelin (1978)	-	-	-	-	81.149	0.014	1476	5
Touzelin (1978)	-	-	-	-	81.262	0.014	1527	5

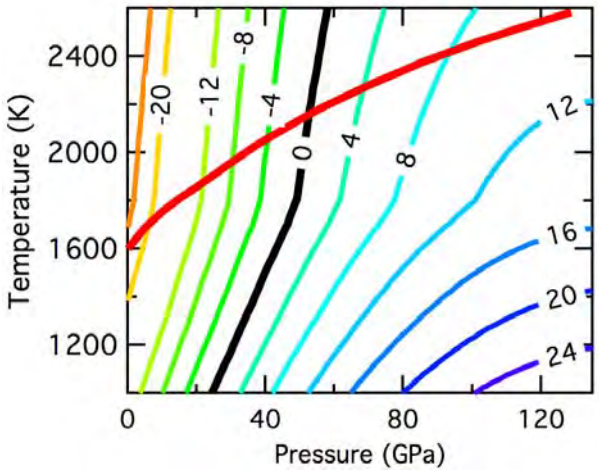

Supplementary Figure 1a. Similar to Figure 4 in the text, but calculated assuming Co metal is more 10% more compressible (K_{0T}=179 GPa). The crossing point with the geotherm lowers by ~10% (to ~53 GPa from ~58 GPa).

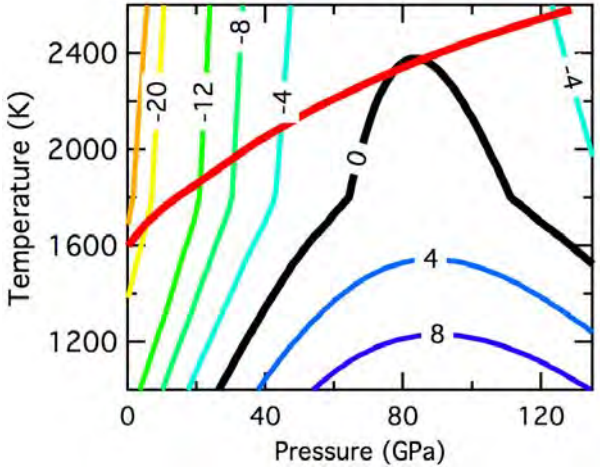

Supplementary Figure 1b Similar to Figure 4, but assuming Co metal is 10% less compressible (K_{0T}=219 GPa). The crossing point with the geotherm moves to higher pressures and exhibits a double crossing behavior (at 77 and 85 GPa).

B2 (100)
B1 (111)
B1 (200)
C (111)
B2 (110)
C (200)
B1 (220)
B2 (200)
C (220)
B1 (222)
Detector azimuth
6
8
10
12
14
2θ (degrees)

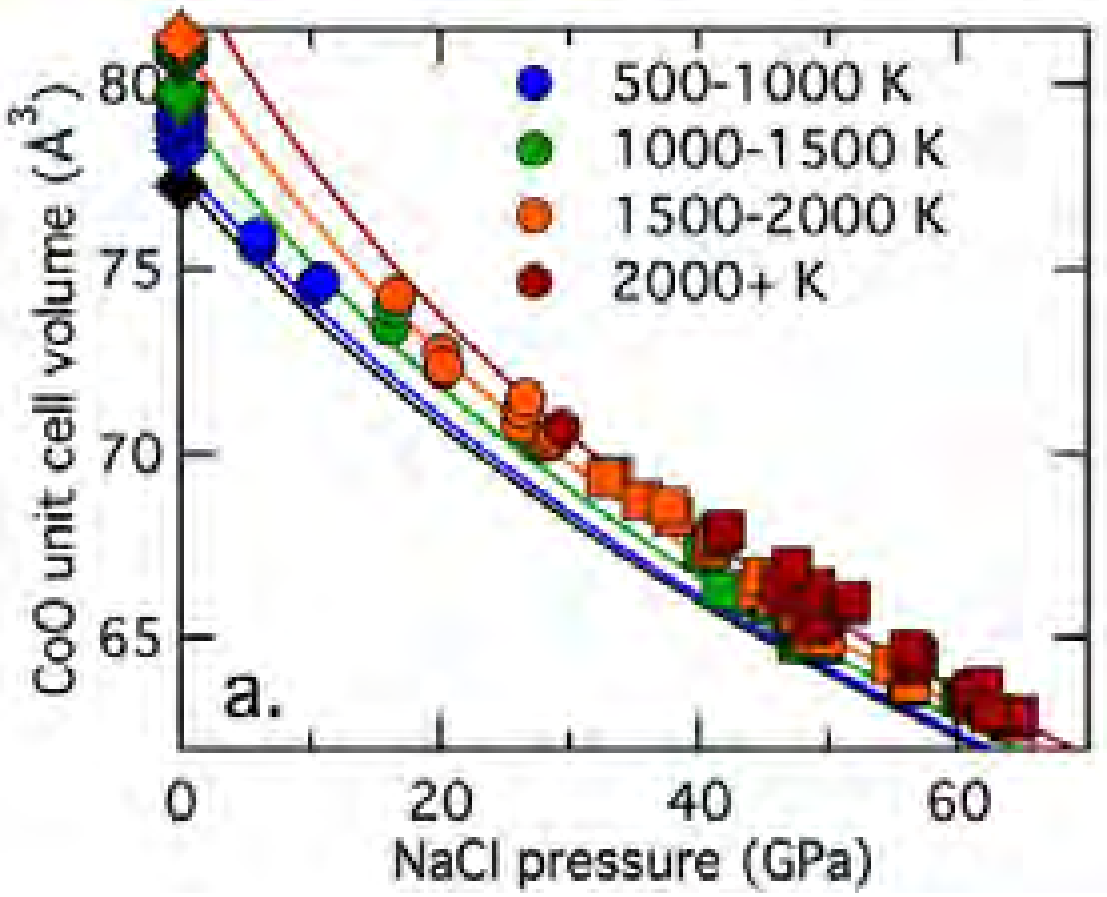
500-1000 K
1000-1500 K
1500-2000 K
2000+ K
CoO unit cell volume (Å^3)
80
75
70
65
a.
0
20
40
60
NaCl pressure (GPa)

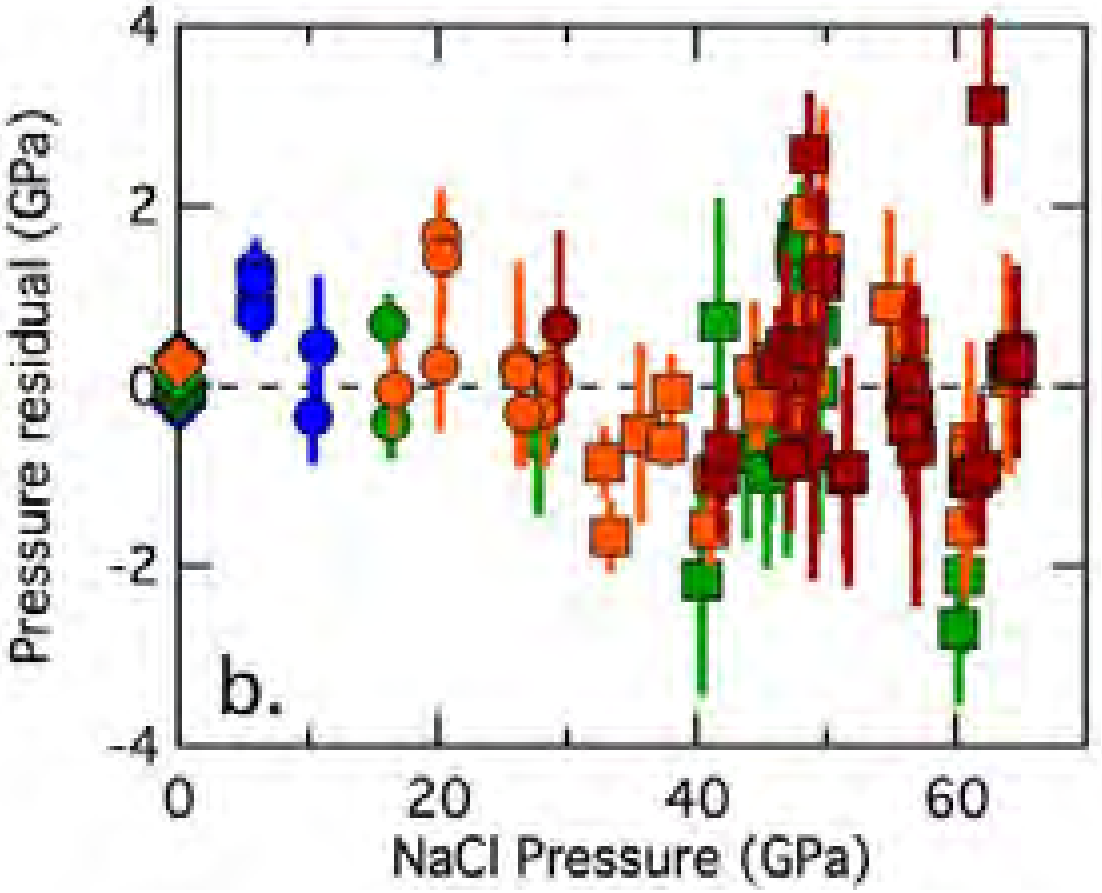
4
2
0
-2
-4
Pressure residual (GPa)
b.
0
20
40
60
NaCl Pressure (GPa)

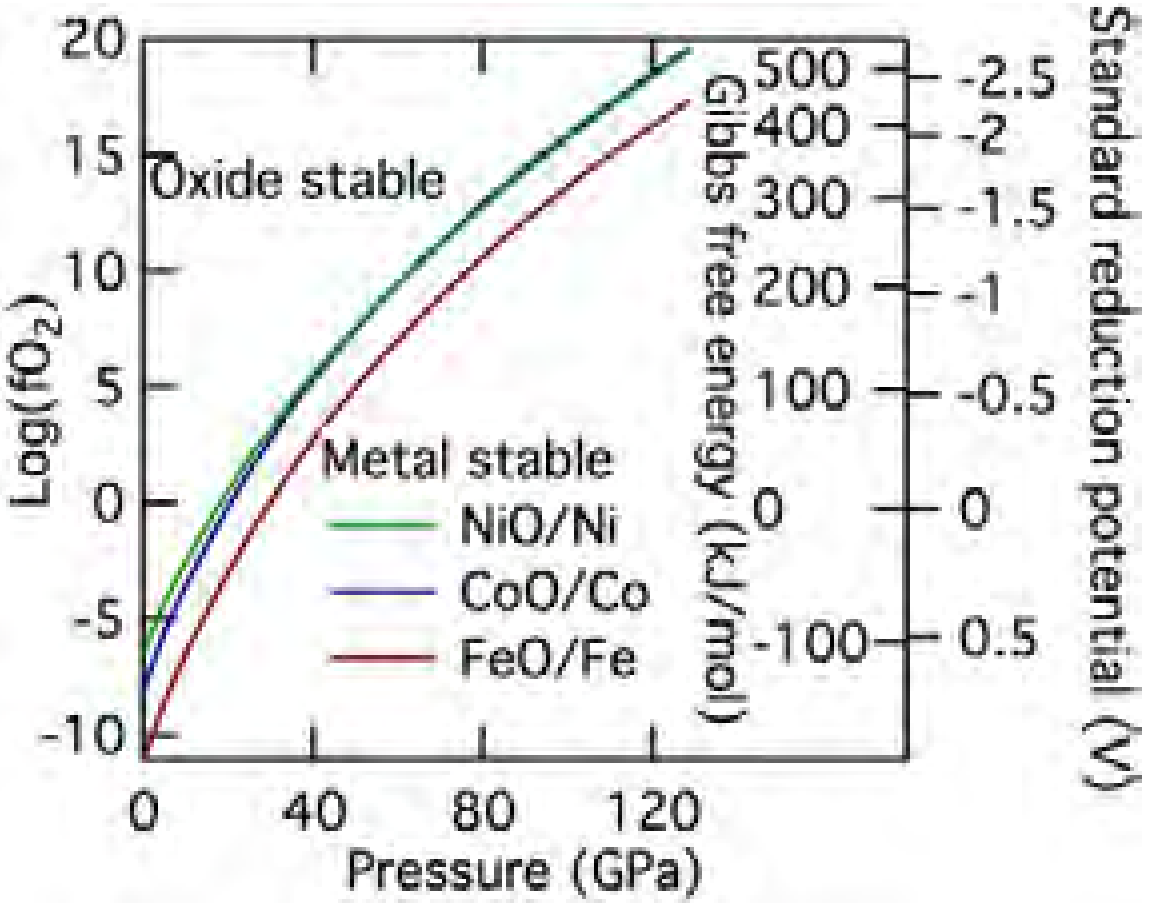
Oxide stable
Metal stable
NiO/Ni
CoO/Co
FeO/Fe
Log(fO2)
Pressure (GPa)
Gibbs free energy (kJ/mol)
Standard reduction potential (V)
20
15
10
5
0
-5
-10
0
40
80
120
500
400
300
200
100
0
-100
-2.5
-2
-1.5
-1
-0.5
0
0.5

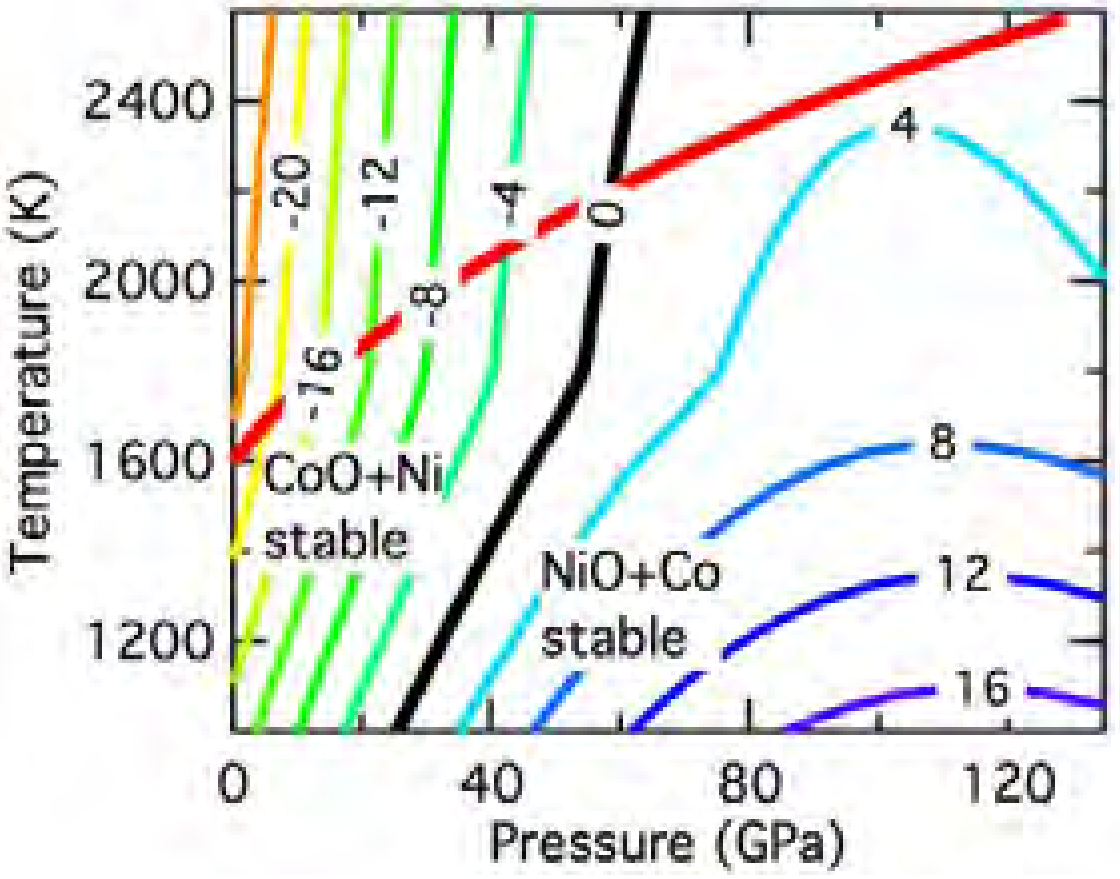
Temperature (K)
2400
2000
1600
1200
0
40
80
120
Pressure (GPa)
-20
-16
-12
-8
-4
0
4
8
12
16
CoO+Ni
stable
NiO+Co
stable

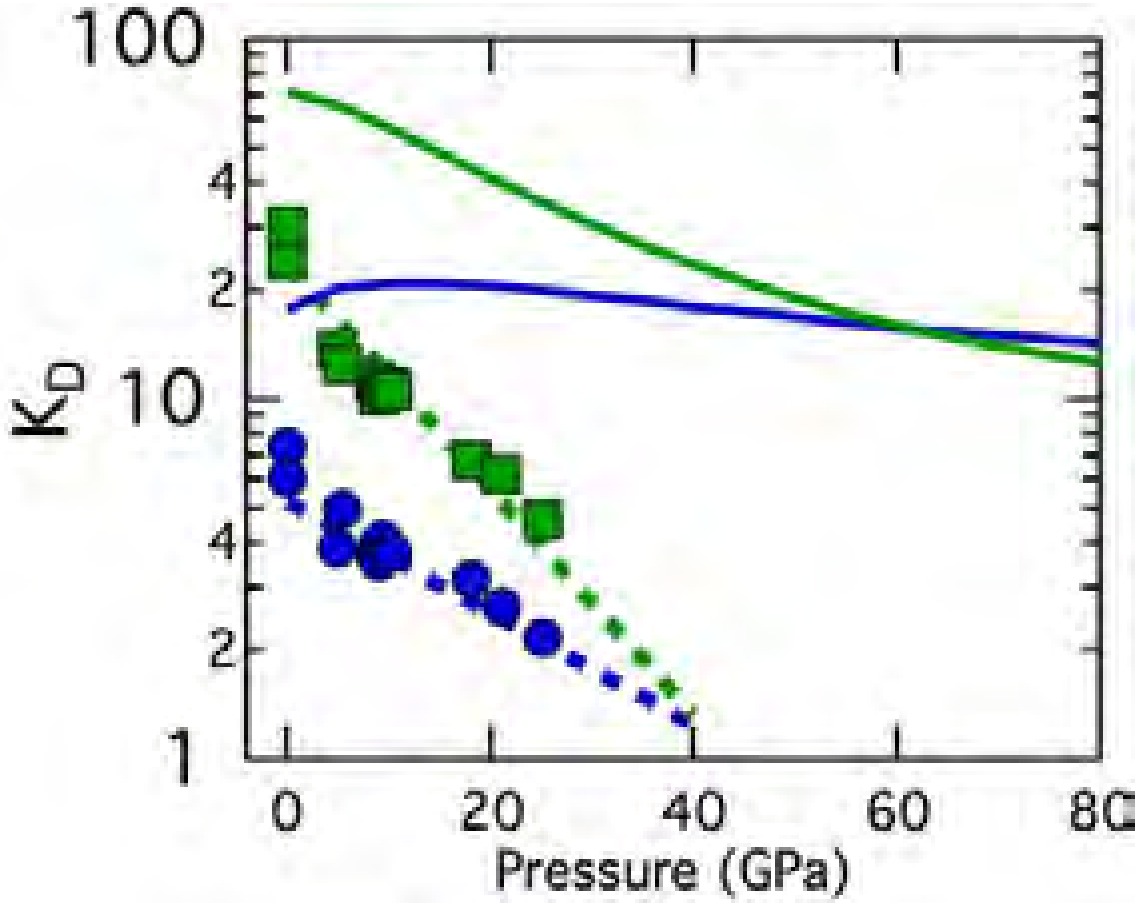
100
4
2
K_D 10
4
2
1
0
20
40
60
80
Pressure (GPa)